Effect of fluid inertia on the orientation of a small prolate spheroid settling in turbulence

K. Gustavsson, M Z Sheikh, D Lopez, A. Naso, A. Pumir, B Mehlig

New Journal of Physics
The open access journal at the forefront of physics

Deutsche Physikalische Gesellschaft DPG IOP Institute of Physics

PAPER • OPEN ACCESS

Effect of fluid inertia on the orientation of a small prolate spheroid settling in turbulence

To cite this article: K Gustavsson *et al* 2019 *New J. Phys.* **21** 083008

New Journal of Physics
The open access journal at the forefront of physics

Deutsche Physikalische Gesellschaft DPG
IOP Institute of Physics

Published in partnership with: Deutsche Physikalische Gesellschaft and the Institute of Physics

OPEN ACCESS

RECEIVED
31 March 2019

REVISED
6 June 2019

ACCEPTED FOR PUBLICATION
9 July 2019

PUBLISHED
5 August 2019

PAPER

Effect of fluid inertia on the orientation of a small prolate spheroid settling in turbulence

K Gustavsson[1], **M Z Sheikh**[2], **D Lopez**[3], **A Naso**[3], **A Pumir**[2,4] **and B Mehlig**[1]

[1] Department of Physics, Gothenburg University, SE-41296 Gothenburg, Sweden
[2] Univ. Lyon, ENS de Lyon, Univ. Claude Bernard, CNRS, Laboratoire de Physique, F-69342, Lyon, France
[3] Univ. Lyon, Ecole Centrale de Lyon, Univ. Claude Bernard, CNRS, INSA de Lyon, Laboratoire de Mécanique des Fluides et d'Acoustique, F-69134, Ecully, France
[4] Max-Planck Institute for Dynamics and Self-Organization, D-37077, Göttingen, Germany

E-mail: bernhard.mehlig@physics.gu.se

Keywords: turbulence, non-spherical particles, angular dynamics, settling, ice crystals in cumulus clouds

Abstract

We study the angular dynamics of small non-spherical particles settling in a turbulent flow, such as ice crystals in clouds, aggregates of organic material in the oceans, or fibres settling in turbulent pipe flow. Most solid particles encountered in Nature are not spherical, and their orientations affect their settling speeds, as well as their collision and aggregation rates in suspensions. Whereas the random action of turbulent eddies favours an isotropic distribution of orientations, gravitational settling breaks the rotational symmetry. The precise nature of the symmetry breaking, however, is subtle. We demonstrate here that the fluid-inertia torque plays a dominant role in the problem. As a consequence rod-like particles tend to settle in turbulence with horizontal orientation, the more so the larger the settling number Sv (a dimensionless measure of the settling speed). For large Sv we determine the fluctuations around this preferential horizontal orientation for prolate particles with arbitrary aspect ratios, assuming small Stokes number St (a dimensionless measure of particle inertia). Our theory is based on a statistical model representing the turbulent velocity fluctuations by Gaussian random functions. This overdamped theory predicts that the orientation distribution is very narrow at large Sv, with a variance proportional to Sv^{-4}. By considering the role of particle inertia, we analyse the limitations of the overdamped theory, and determine its range of applicability. Our predictions are in excellent agreement with numerical simulations of simplified models of turbulent flows. Finally we contrast our results with those of an alternative theory predicting that the orientation variance is proportional to Sv^{-2} at large Sv.

1. Introduction

The settling of particles in turbulence is important in a wide range of scientific problems. An example is the settling of small ice crystals in clouds [1]. The orientation of small ice crystals has manifestly a direct impact on the reflection properties of electromagnetic waves (including light) from clouds [2–4], with potentially important consequences for the albedo and the climate. In addition, it was noted that the dispersion in the orientation of identical crystals leads to differences in their settling velocities, which in turn affects the collision and aggregation rates [5, 6], essential in the formation of precipitation. A second example highlighting the significance of particles settling in turbulence is the dynamics of small aggregates of organic matter in the oceans ('marine snow') [7]. The interaction of settling and turbulence also affects the dynamics of swimming of microorganisms [8–10] in the oceanographic context. A problem of industrial relevance is the wall-deposition of fibres in a turbulent pipe flow [11].

The settling of spherical particles in turbulence has been intensively studied. Maxey and collaborators [12–14] found that turbulence increases the settling speed of small spherical particles. This pioneering work has led to many experimental and numerical studies, using direct numerical simulation (DNS) of turbulence, and it is a question of substantial current interest [15, 16]. An important question is how frequently particles collide as

they settle in turbulence [17, 18]. The collision rate is influenced by spatial inhomogeneities in the particle-number density due to the effect of particle inertia. There is substantial recent progress in understanding this two-particle problem [19–23]. The conclusion is that settling may increase or decrease spatial clustering of spherical particles, and that it tends to decrease the relative velocities of nearby particles because settling reduces the frequencies of 'caustics', singularities in the inertial-particle dynamics [19].

Most solid particles encountered in Nature and in Engineering are not spherical, yet less is known about the settling of non-spherical particles in turbulence, and their settling depends in an essential way on their orientation. In a fluid at rest the orientation of a slowly settling non-spherical particle is determined by weak torques induced by the convective inertia of the fluid—set in motion by the moving particle. For a single, isolated particle in a quiescent fluid this effect is well understood [24–27]: convective fluid inertia due to slip between the particle and the fluid velocity causes non-spherical particles to settle with their broad side first. For axisymmetric rods, for example, symmetry dictates that the angular dynamics has two equilibrium orientations: either the rod is aligned with gravity (tip first) or perpendicular to gravity. At weak inertia, only the latter orientation is stable, so that the rod settles with its long edge first. But when there is turbulence, then turbulent vorticity and strain exert additional torques that cause fluctuations in the orientations of the settling crystals [1, 28].

To understand the angular motion of a non-spherical particle settling in turbulence is in general a very complex problem, because there are many dimensionless parameters to consider. There is particle shape (shape parameter Λ), and the effect of particle inertia is measured by the Stokes number St. The importance of settling is determined by Sv, a dimensionless measure of the settling speed. The significance of fluid inertia is quantified by two Reynolds numbers, the particle Reynolds number Re_p (convective inertia due to slip between particle and fluid velocity), and the shear Reynolds number Re_s (convective inertia due to fluid-velocity gradients). The nature of the turbulent velocity fluctuations is determined by the Taylor-scale Reynolds number Re_λ.

If the particles are so small that they just follow the flow and that any inertial corrections to the fluid torque are negligible ($\mathrm{Re}_p = \mathrm{Re}_s = 0$), then the angular dynamics of small crystals in turbulence is well understood [10, 29–38]. The particle orientation responds to local vorticity and strain through Jeffery's equation [29]. The effect of particle inertia is straightforward to take into account [39], but the role of fluid inertia is more difficult to describe, even in the absence of settling. In certain limiting cases fluid-inertial effects are well understood. The most important example is that of a small neutrally buoyant ($\mathrm{Re}_s = \mathrm{St}$) spheroid moving in a time-independent linear shear flow, so that the centre-of-mass of the particle follows the flow ($\mathrm{Re}_p = 0$). Neglecting inertial effects ($\mathrm{Re}_s = 0$) and angular diffusion, the angular dynamics degenerates into a one-parameter family of marginally stable orbits, the so-called Jeffery orbits [29]. Fluid inertia breaks this degeneracy and gives rise to certain stable orbits [40–43]. Much less is known when Re_p is not zero. Candelier, Mehlig and Magnaudet [44] recently showed how to compute the effect of a small slip upon the force and torque on a non-spherical particle in a general linear time-independent flow, by generalising Saffman's result [45, 46] on the lift upon a small sphere in a shear flow, valid in the limit where $\mathrm{Re}_p \ll \sqrt{\mathrm{Re}_s} \ll 1$.

The results summarised in the previous paragraph pertain to time-independent flows. Time-dependent spatially inhomogeneous flows present new challenges, and very little is known about the effect of fluid inertia for such flows, in particular for turbulence. In some studies, therefore, effects of fluid inertia were simply neglected [5, 6, 47–49]. These models predict that the breaking of isotropy due to gravity causes a bias in the orientation distribution of the settling particles, so that rods tend to settle tip first, parallel to gravity. For small particles it is safe to neglect Re_s [50]. But experiments and numerical simulations of slender particles settling in a vortex flow [51] and in turbulence [52] show that convective inertial torques due to settling can make a qualitative difference to the orientation distribution.

In this paper we therefore consider the effect of the convective inertial torques on the orientation of small spheroids settling in turbulence. Following [51], our model assumes that the hydrodynamic torque is approximately given by the sum of Jeffery's torque and the convective inertial torque in a homogeneous, time-independent flow. For nearly spherical particles this convective torque was calculated by Cox [24], and for slender bodies by Khayat and Cox [25]. Their results were generalised to spheroids with arbitrary aspect ratios in [26].

Our goal is to analyse how the turbulent-velocity fluctuations affect the orientation distribution of a prolate spheroid settling through turbulence. We assume that the particles are small enough so that convective-inertia effects due to the fluid-velocity gradients are negligible, that inertial effects on the centre-of-mass motion are small (small St and Re_p), but that the settling number Sv is large enough so that the fluid-inertia torque dominates the angular dynamics.

We find an approximate theory for the angular distribution of settling spheroids using a statistical model [48, 53] for the turbulent fluctuations. The theory is valid for large Sv and small St, in the overdamped limit, and its predictions are in excellent agreement with results of numerical simulations of the statistical model, and with simulations using a kinematic-simulation (KS) model [54, 55] for the turbulent flow. We find that the variance of the orientation is proportional to Sv^{-4} in the limit of large settling number Sv, for small enough Stokes

number St, and the theory determines how the pre-factor depends on the shape of the spheroid. In the slender-body limit, the Sv^{-4}-scaling of the variance was also found in [56] using an approach equivalent to ours.

We contrast our results with a theory for the orientation variance derived by Klett [28] for nearly spherical particles. This theory predicts that the variance is proportional to Sv^{-2}. At first sight this may appear to be at variance with the overdamped theory, but we show that the overdamped approximation breaks down into several different regimes when particle inertia begins to matter. At very large values of Sv, when the time scale at which the fluid-velocity gradients decorrelate is the smallest time scale of the inertial dynamics, our numerical simulations show a Sv^{-2}-scaling, as suggested by Klett's theory. But the theory is difficult to justify because it neglects particle inertia in the centre-of-mass dynamics. Our numerical simulations demonstrate that translational particle inertia has a significant effect upon the angular dynamics, indicating that it must be taken into account as soon as the overdamped approximation for the angular dynamics breaks down.

The remainder of this paper is organised as follows. In section 2 we describe our model: the approximate equations of motion and the statistical model for the turbulent-velocity fluctuations. In section 3 we show results of numerical simulations of our model. We describe how and why the results differ from those in [5, 6, 47–49], and explain the intuition behind our theory for small St and large Sv. The overdamped theory is described in section 4. Section 5 discusses the effect of particle inertia, and section 6 contains our conclusions as well as an outlook.

2. Model

2.1. Particle equation of motion

Newton's equations of motion for a single non-spherical particle read:

$$m_\mathrm{p}\dot{\boldsymbol{v}}_\mathrm{p} = \boldsymbol{f} + m_\mathrm{p}\boldsymbol{g}, \quad \dot{\boldsymbol{x}}_\mathrm{p} = \boldsymbol{v}_\mathrm{p}, \tag{1a}$$

$$m_\mathrm{p}\frac{\mathrm{d}}{\mathrm{d}t}[\mathbb{I}_\mathrm{p}(\boldsymbol{n})\boldsymbol{\omega}_\mathrm{p}] = \boldsymbol{\tau}, \quad \dot{\boldsymbol{n}} = \boldsymbol{\omega}_\mathrm{p} \wedge \boldsymbol{n}. \tag{1b}$$

Here $\boldsymbol{g}$ is the gravitational acceleration with direction $\hat{\boldsymbol{g}} = \boldsymbol{g}/|\boldsymbol{g}|$, $\boldsymbol{x}_\mathrm{p}$ is the position of the particle, $\boldsymbol{v}_\mathrm{p}$ its centre-of-mass velocity, m_p the particle mass, and the dots denote time derivatives. We assume that the particle is axisymmetric, so that its orientation is characterised by the unit vector $\boldsymbol{n}$ along the symmetry axis of the particle. The angular velocity of the particle is denoted by $\boldsymbol{\omega}_\mathrm{p}$, and $\mathbb{I}_\mathrm{p}(\boldsymbol{n})$ is its rotational inertia tensor per unit-mass in the lab frame. For a spheroid, the elements of $\mathbb{I}_\mathrm{p}(\boldsymbol{n})$ are given by [57]

$$(\mathbb{I}_\mathrm{p})_{ij}(\boldsymbol{n}) = I_\perp(\delta_{ij} - n_i n_j) + I_\parallel n_i n_j, \quad I_\perp = \frac{1+\lambda^2}{5}a_\perp^2, \quad I_\parallel = \frac{2}{5}a_\perp^2, \tag{2}$$

where $\lambda \equiv a_\parallel/a_\perp$ is the aspect ratio of the spheroid, $2a_\parallel$ is the length of the symmetry axis, and $2a_\perp$ is the diameter of the spheroid. Prolate spheroids correspond to $\lambda > 1$, whereas oblate spheroids have $\lambda < 1$.

The difficulty lies in computing the hydrodynamic force $\boldsymbol{f}$ and torque $\boldsymbol{\tau}$ on the particle. In the Stokes approximation, unsteady and convective inertial effects are neglected. In this creeping-flow limit [57], the force and torque exerted by a steady flow upon the spheroid are linearly related to the slip velocity $\boldsymbol{W} \equiv \boldsymbol{v}_\mathrm{p} - \boldsymbol{u}$, to the angular slip velocity $\boldsymbol{\omega}_\mathrm{p} - \boldsymbol{\Omega}$, and to the fluid strain $\mathbb{S}$:

$$\begin{bmatrix} \boldsymbol{f}^{(0)} \\ \boldsymbol{\tau}^{(0)} \end{bmatrix} = 6\pi a_\perp \mu \begin{bmatrix} \mathbb{A} & 0 & 0 \\ 0 & \mathbb{C} & \mathbb{H} \end{bmatrix} \begin{bmatrix} \boldsymbol{u} - \boldsymbol{v}_\mathrm{p} \\ \boldsymbol{\Omega} - \boldsymbol{\omega}_\mathrm{p} \\ \mathbb{S} \end{bmatrix}. \tag{3}$$

Here μ is the dynamic viscosity of the fluid, $\boldsymbol{u} \equiv \boldsymbol{u}(\boldsymbol{x}_\mathrm{p}, t)$ is the undisturbed fluid velocity at the particle position $\boldsymbol{x}_\mathrm{p}$, $\boldsymbol{\Omega} \equiv \frac{1}{2}\boldsymbol{\nabla} \wedge \boldsymbol{u}$ is half the vorticity of the undisturbed fluid-velocity field at the particle position, and $\mathbb{S}$ is the strain-rate matrix, the symmetric part of the matrix of the undisturbed fluid-velocity gradients (its antisymmetric part is denoted by $\mathbb{O}$). The tensors $\mathbb{A}$, $\mathbb{C}$, and $\mathbb{H}$ are translational and rotational resistance tensors. Their forms are determined by the shape of the particle. Equation (3) shows that the tensor $\mathbb{A}$ relates the hydrodynamic force $\boldsymbol{f}^{(0)}$ to the slip velocity $\boldsymbol{W}$. For an axisymmetric particle with fore-aft symmetry the tensor takes the form

$$A_{ij} \equiv A_\perp(\delta_{ij} - n_i n_j) + A_\parallel n_i n_j. \tag{4}$$

The resistance coefficients $A_\perp$ and $A_\parallel$ depend on the shape of the particle. For a spheroid, they are given by [57]:

$$A_\perp = \frac{8(\lambda^2-1)}{3\lambda[(2\lambda^2-3)\beta+1]}, \; A_\parallel = \frac{4(\lambda^2-1)}{3\lambda[(2\lambda^2-1)\beta-1]},$$
$$\text{with } \beta = \frac{\ln[\lambda + \sqrt{\lambda^2-1}\,]}{\lambda\sqrt{\lambda^2-1}}. \tag{5}$$

For a sphere one has $A_\perp = A_\parallel = 1$, so that $\boldsymbol{f}^{(0)}$ simplifies to the expression for Stokes force on a sphere moving with velocity $\boldsymbol{v}_\mathrm{p}$ through a fluid with velocity $\boldsymbol{u}$.

In the creeping-flow limit, the steady slip velocity $\boldsymbol{W}$ of a spheroid subject to a gravitational force $m_\mathrm{p}\boldsymbol{g}$ is obtained by setting the acceleration $\dot{\boldsymbol{v}}_\mathrm{p}$ to zero in equation (1*a*):

$$\boldsymbol{W}^{(0)} = \tau_\mathrm{p}[A_\perp^{-1}(\mathbb{1} - \boldsymbol{n}\boldsymbol{n}^\mathsf{T}) + A_\parallel^{-1}\boldsymbol{n}\boldsymbol{n}^\mathsf{T}]\boldsymbol{g}. \tag{6}$$

Here $\mathbb{1}$ is the unit matrix, and $\tau_\mathrm{p} \equiv (2a_\parallel a_\perp \rho_\mathrm{p})/(9\nu\rho_\mathrm{f})$ is the particle response time in Stokes' approximation with kinematic viscosity $\nu = \mu/\rho_\mathrm{f}$, fluid-mass density ρ_f, and particle-mass density ρ_p. The slip velocity depends on the orientation $\boldsymbol{n}$ of the particle.

For an axisymmetric particle with fore-aft symmetry, the rotational resistance tensors take the form:

$$C_{ij} \equiv C_\perp(\delta_{ij} - n_i n_j) + C_\parallel n_i n_j \quad \text{and } H_{ijk} = H_0\epsilon_{ijl}n_k n_l. \tag{7}$$

Here ϵ_{ijl} is the anti-symmetric Levi-Civita tensor, and we use the Einstein summation convention: repeated indices are summed from 1 to 3. For a spheroid, the rotational resistance coefficients read [57]:

$$C_\perp = \frac{8a_\parallel a_\perp(\lambda^4 - 1)}{9\lambda^2[(2\lambda^2 - 1)\beta - 1]},\ C_\parallel = -\frac{8a_\parallel a_\perp(\lambda^2 - 1)}{9(\beta - 1)\lambda^2},$$
$$H_0 = -C_\perp\frac{\lambda^2 - 1}{\lambda^2 + 1}. \tag{8}$$

Expressions (3)–(8) determine the hydrodynamic force and torque in the creeping-flow limit. Fluid-inertia effects are neglected in $\boldsymbol{f}^{(0)}$ and $\boldsymbol{\tau}^{(0)}$.

There are two distinct corrections when fluid-inertia effects are weak but not negligible, due to the undisturbed fluid-velocity gradients, $\mathbb{S}$ and $\mathbb{O}$, and due to the slip velocity $\boldsymbol{W}$. The former are parameterised by the shear Reynolds number Re_s, the latter by the particle Reynolds number Re_p:

$$\mathrm{Re}_s = \frac{sa^2}{\nu} \quad \text{and } \mathrm{Re}_p = \frac{W_\perp^{(0)}a}{\nu}. \tag{9}$$

Here $a = \max\{a_\perp, a_\parallel\}$ is the largest dimension of the particle, and $W_\perp^{(0)}$ is an estimate of the slip velocity: the magnitude of the velocity of a small slender spheroidal particle settling under gravity in a quiescent fluid with its symmetry axis perpendicular to gravity. From equation (6) we see that $W_\perp^{(0)} = \tau_\mathrm{p}g/A_\perp$. In the definition of Re_s, the parameter s is a characteristic shear rate. In turbulence it is on average of the order $s \sim \tau_\mathrm{K}^{-1}$ where τ_K is the Kolmogorov time

$$\tau_\mathrm{K} = (2\langle \mathrm{Tr}\,\mathbb{S}\mathbb{S}^\mathsf{T}\rangle)^{-1/2} \sim (\nu/\mathscr{E})^{1/2}. \tag{10}$$

Here the average $\langle\cdots\rangle$ is over Lagrangian fluid trajectories, and $\mathscr{E}$ is the turbulent dissipation rate per unit mass. This yields the estimate [50] $\mathrm{Re}_s \sim (a/\eta_K)^2$, where

$$\eta_\mathrm{K} = \sqrt{\nu\tau_\mathrm{K}} \sim (\nu^3/\mathscr{E})^{1/4} \tag{11}$$

is the Kolmogorov length [58]. Thus the shear Reynolds number is small for small particles.

Now consider the effect of convective inertia. Following [51] we assume that the torque on the particle is given by the sum of Jeffery's torque and the instantaneous convective-inertia torque in a homogeneous flow. This approximation can be strictly justified for a steady linear flow in the limit $\sqrt{\mathrm{Re}_s} \ll \mathrm{Re}_p \ll 1$. In this limit the singular perturbation problem that determines the fluid-inertia torque simplifies: the length scale at which fluid-velocity gradients cause the Stokes approximation to fail (the Saffman length $a/\sqrt{\mathrm{Re}_s}$) is much larger than the length scale where convective fluid inertia causes the Stokes approximation to break down (the Oseen length a/Re_p). This implies that the leading convective-inertial corrections to the torque are those corresponding to a quiescent fluid, and a similar argument can be made for the convective-inertia contribution to the force. While there is no general theory explaining how the convective-inertia contributions to the force and the torque are affected by spatial inhomogeneities in time-dependent flows, the results of [51] show that the simple model used here can successfully explain important features of the orientation distribution of rods settling in a vortex flow.

The leading-order inertial force correction for a heavy spheroid moving in a quiescent fluid reads [25, 59]:

$$\boldsymbol{f}^{(1)} = -(6\pi a_\perp\mu)\tfrac{3}{16}\mathrm{Re}_p\frac{\boldsymbol{W}}{W_\perp^{(0)}}[3\mathbb{A} - \mathbb{I}(\hat{\boldsymbol{W}}\cdot\mathbb{A}\hat{\boldsymbol{W}})]\mathbb{A}\boldsymbol{W}, \tag{12}$$

with $W = |\boldsymbol{W}|$ and $\hat{\boldsymbol{W}} = \boldsymbol{W}/W$. For a spheroid, the corresponding leading-order inertial contribution to the torque was calculated in [26]:

$$\boldsymbol{\tau}^{(1)} = F(\lambda)\mu a^2\,\mathrm{Re}_p\frac{W^2}{W_\perp^{(0)}}(\boldsymbol{n}\cdot\hat{\boldsymbol{W}})(\boldsymbol{n}\wedge\hat{\boldsymbol{W}}). \tag{13}$$

The shape factor $F(\lambda)$ is given in [26]. It is also shown in figure 1(a).

Combining equations (1)–(3) with (12), (13) yields the equations of motion for our model. We use the Kolmogorov time τ_K and the Kolmogorov length η_K to de-dimensionalise the equations of motion, $\boldsymbol{x}' = \boldsymbol{x}/\eta_\mathrm{K}$,

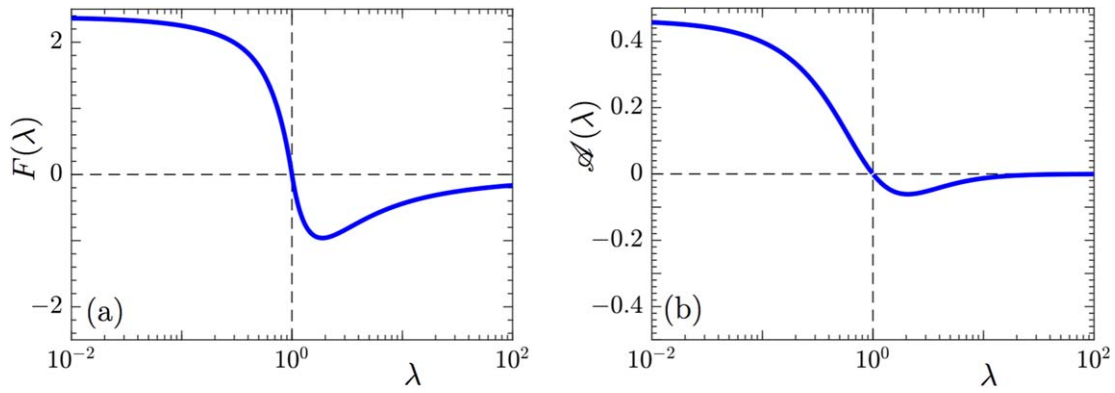

Figure 1. Geometrical shape factors. (a) Shape factor $F(\lambda)$ in equation (13). The data shown are obtained by evaluating equations (4.1) and (4.2) in [26]. (b) Shape factor $\mathscr{A}(\lambda)$ defined in equation (25), as a function of the particle aspect ratio λ.

$t' = t/\tau_K$, $\boldsymbol{v}' = \boldsymbol{v}\tau_K/\eta_K$, $\boldsymbol{\omega}' = \boldsymbol{\omega}\tau_K$. This gives (after dropping the primes):

$$\dot{\boldsymbol{x}}_p = \boldsymbol{v}_p, \tag{14a}$$

$$\dot{\boldsymbol{v}}_p = \frac{1}{\mathrm{St}}\left[-\left(\mathbb{1} + \tfrac{3}{16}\tfrac{a}{\eta_K}W[3\mathbb{A} - \mathbb{I}(\hat{\boldsymbol{W}}\cdot\mathbb{A}\hat{\boldsymbol{W}})]\right)\mathbb{A}W + \mathrm{Sv}\hat{\boldsymbol{g}}\right], \tag{14b}$$

$$\dot{\boldsymbol{n}} = \boldsymbol{\omega}_p \wedge \boldsymbol{n}, \tag{14c}$$

$$\dot{\boldsymbol{\omega}}_p = \frac{1}{\mathrm{St}}[\mathbb{I}_p^{-1}\mathbb{C}(\boldsymbol{\Omega} - \boldsymbol{\omega}_p) + \mathbb{I}_p^{-1}\mathbb{H}\colon\mathbb{S} + \mathscr{A}'(\boldsymbol{n}\cdot W)(\boldsymbol{n}\wedge W)] + \Lambda(\boldsymbol{n}\cdot\boldsymbol{\omega}_p)(\boldsymbol{\omega}_p\wedge\boldsymbol{n}). \tag{14d}$$

Equations (14) have four independent dimensionless parameters:

$$\Lambda = \frac{\lambda^2-1}{\lambda^2+1}, \quad \frac{a}{\eta_K}, \quad \mathrm{St} = \frac{\tau_p}{\tau_K}, \quad \mathrm{Sv} = \frac{g\tau_p\tau_K}{\eta_K}. \tag{15}$$

Here Λ is the shape parameter that appears in Jeffery's equation, and Sv is the settling number [60], a dimensionless measure of the settling speed. It is proportional to the particle size squared, a^2, just as the Stokes number.

The shape-dependent prefactors in equation (14) are combinations of the parameters defined in equations (2), (7) and (8)

$$[\mathbb{I}_p^{-1}\mathbb{C}]_{ij} = \frac{C_\perp}{I_\perp}(\delta_{ij} - n_in_j) + \frac{C_\parallel}{I_\parallel}n_in_j, \quad [\mathbb{I}_p^{-1}\mathbb{H}]_{ijk} = -\frac{C_\perp\Lambda}{I_\perp}\epsilon_{ijl}n_kn_l, \tag{16}$$

as well as

$$\mathscr{A}' = \frac{5}{6\pi}F(\lambda)\frac{\max(\lambda,\,1)^3}{\lambda^2+1}. \tag{17}$$

The Reynolds number Re_p does not appear explicitly in equations (14) because we made the equations of motion dimensionless by scaling time and length with the Kolmogorov scales τ_K and η_K. If we use an estimate of the slip velocity instead (such as $W_\perp^{(0)}$), then Re_p features in the dimensionless equations of motion. The latter convention is used in [25, 26], and more generally in perturbative calculations of weak inertial effects on the motion of particles in simple flows [44–46, 61]. These two different choices must lead to equivalent equations of motion, but our scheme has the advantage that it emphasises the different roles played by $\boldsymbol{f}^{(1)}$ and $\boldsymbol{\tau}^{(1)}$ for small particles in turbulence. Equation (14*b*) shows that the fluid-inertia contribution to the force, $\boldsymbol{f}^{(1)}$, is multiplied by the dimensionless prefactor a/η_K. This means that $\boldsymbol{f}^{(1)}$ makes only a small contribution for small enough particles, which we do not expect to qualitatively change the results derived below. In the following we therefore neglect this contribution (although it could be taken into account in simulations and theory). More importantly, the fluid-inertia contribution to the torque in equation (14*d*) has no such factor. The fluid-inertia torque is of the same order as the Jeffery torque. This means that the fluid-inertia contribution to the torque may be substantial for small particles, even though the fluid-inertia correction to the force is negligible. This difference can be traced back to the different particle-size dependencies of the translational and angular accelerations. Equations (1) and (3) show that the Stokes acceleration is proportional to $m_p^{-1}|\boldsymbol{f}^{(0)}| \sim a^{-2}$, while the inertial correction to the translational acceleration is proportional to $m_p^{-1}|\boldsymbol{f}^{(1)}| \sim a^{-1}$, parametrically smaller than the Stokes acceleration for small particles. For the angular accelerations we find: $m_p^{-1}|\mathbb{I}_p^{-1}\boldsymbol{\tau}^{(0)}| \sim a^{-2}$, and $m_p^{-1}|\mathbb{I}_p^{-1}\boldsymbol{\tau}^{(1)}| \sim a^{-2}$, of the same order (these dependencies are consistent with equation (14) since $\mathrm{St}^{-1} \sim a^{-2}$). As a consequence, fluid-inertia effects

may play a prevalent role in the orientation of small ice crystals settling in highly turbulent flows. In particular, at large Sv the particle settles rapidly so that W is large. In this limit one therefore expects the fluid-inertia torque $\boldsymbol{\tau}^{(1)}$ to dominate over Jeffery's torque $\boldsymbol{\tau}^{(0)}$, so that the inertial torque cannot be neglected (as was done in [5, 6, 47–49]). It is argued in [62] that the orientation bias predicted in [5, 47, 48] can possibly be observed in small-Re_λ flow, but not at high Re_λ.

In the following we neglect the contribution from $\boldsymbol{f}^{(1)}$. At the same time we assume that the settling speed is so large that the fluid-inertia torque $\boldsymbol{\tau}^{(1)}$ dominates the angular dynamics. If there was no flow, the particles would settle with their broad side first in this limit. The question is how turbulent fluctuations modify the orientation distribution of the settling particles.

2.2. Statistical model

In our theory we use a statistical model [53] to represent the turbulent fluctuations. We model the incompressible homogeneous and isotropic turbulent fluid-velocity field $\boldsymbol{u}(\boldsymbol{x},\, t)$ as a Gaussian random function with correlation length ℓ, correlation time τ, and root-mean-square magnitude u_0 (here and in section 2.3 we write the equations in dimensional form because we want to make explicit how these scales are related to the Kolmogorov scales). Following [53] we express the fluid-velocity field $\boldsymbol{u}(\boldsymbol{x},\, t)$ in three spatial dimensions (3D) as

$$\boldsymbol{u} = \mathcal{N}_3\, \boldsymbol{\nabla} \wedge \boldsymbol{A}. \tag{18}$$

The components A_j of the vector field $\boldsymbol{A}$ are Gaussian random functions with mean zero, $\langle A_j(\boldsymbol{x},\, t)\rangle = 0$, and with correlation functions

$$\langle A_i(\boldsymbol{x},\, t) A_j(\boldsymbol{x}',\, t')\rangle = \delta_{ij}\ell^2 u_0^2 \exp\left(-\frac{|\boldsymbol{x}-\boldsymbol{x}'|^2}{2\ell^2} - \frac{|t-t'|}{\tau}\right). \tag{19}$$

We choose the normalisation $\mathcal{N}_3 = 1/\sqrt{6}$ so that $u_0 = \sqrt{\langle |\boldsymbol{u}|^2\rangle}$. Below we also quote results for a two-dimensional (2D) version of this model. In this case we take

$$\boldsymbol{u} = \mathcal{N}_2 \begin{bmatrix} \partial_2 A_3 \\ -\partial_1 A_3 \end{bmatrix} \tag{20}$$

with $\mathcal{N}_2 = 1/\sqrt{2}$, and where ∂_j represents the derivative with respect to the spatial coordinate x_j. As the equation of motion for the 2D model we use equation (14) with $\boldsymbol{n}$ and the translational dynamics constrained to the flow plane.

The statistical model has an additional dimensionless parameter, the Kubo number $\mathrm{Ku} = u_0\tau/\ell$ [53]. Evaluating equation (10) in the statistical model gives (section 5.1 in [53]):

$$\frac{\tau}{\tau_\mathrm{K}} = \sqrt{d+2}\ \mathrm{Ku}, \tag{21}$$

where d is the spatial dimension. Equation (21) implies that $\tau_\mathrm{K} \ll \tau$ in the limit of large Ku. This means that the relevant time scale of the flow is τ_K: the fluid-velocity gradients sampled along particle trajectories decorrelate due to the spatial displacement of the particle rather than because of temporal changes of the fluid velocity. In the limit of large Ku the model therefore becomes independent of τ. Consequently the exact value of Ku no longer matters as long as it is finite (so that the flow is not frozen). One must use the limit of large Ku to model small-scale fluid-velocity fluctuations in the dissipative range of homogeneous isotropic turbulence, because the turbulent velocity gradients decorrelate on the time scale τ_K, as in the statistical model for large Ku. We emphasise that the small-scale fluid-velocity fluctuations in turbulence are universal [63] but not Gaussian, contrary to the statistics assumed in the statistical model. The non-Gaussian character increases as the Reynolds number increases [64]. Nevertheless, earlier comparisons between results from the statistical model and DNS often show a qualitative or even quantitative agreement [10, 48, 53, 65–67]. The spatial correlation length ℓ satisfies $\ell^2 = \langle u_1^2\rangle / \langle (\partial_1 u_1)^2\rangle$, which defines the Taylor length scale [58] in turbulence. The length scale ℓ is related to the Kolmogorov length by [58, 68]

$$\frac{\ell}{\eta_\mathrm{K}} = \mathscr{C}\sqrt{\mathrm{Re}_\lambda}, \tag{22}$$

where $\mathscr{C}$ is a constant of order unity. The ratio ℓ/η_K (or alternatively the Taylor-scale Reynolds number Re_λ) constitutes a sixth dimensionless parameter of the model, in addition to the Kubo number and the four parameters listed in equation (15). In all statistical-model simulations described in this paper we set $\mathrm{Ku} = 10$ and $\ell/\eta_\mathrm{K} = 10$, and we determine the parameters τ and ℓ of the statistical model from equations (21), (22).

The statistical model is constructed to approximate the dissipative-range fluctuations of 3D turbulence [53]. We note that the predictions of the 2D and 3D statistical models are essentially similar, but the 2D model is easier to analyse, and it can be simulated more accurately. Two- and three-dimensional turbulence, by contrast, exhibit significantly different fluid-velocity fluctuations.

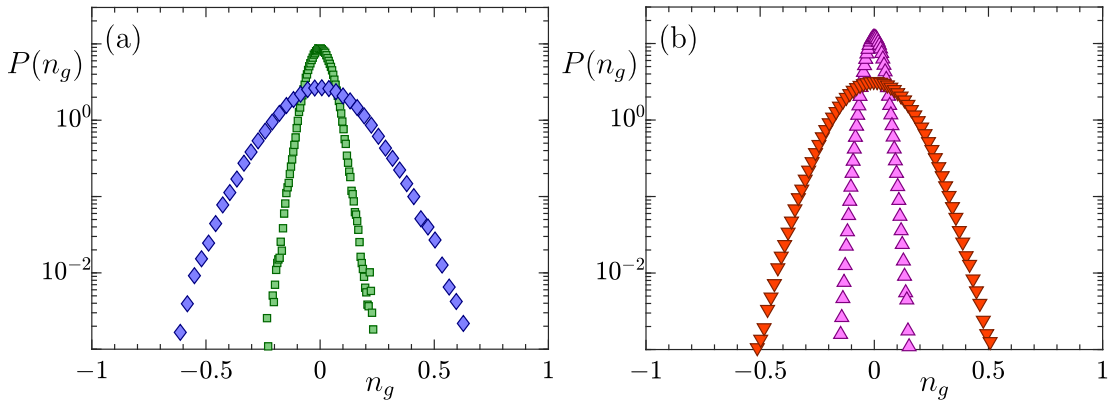

Figure 2. Distribution of $n_g = \boldsymbol{n} \cdot \hat{\boldsymbol{g}}$ obtained by three-dimensional statistical-model simulations of equation (14) for rod-like particles with aspect ratio $\lambda = 5$. (a) Settling number Sv = 18, Stokes numbers St = 0.22 (green, □) and St = 1.1 (blue, ◇). (b) Sv = 45, St = 0.22 (magenta, △) and St = 2.2 (red, ▽).

2.3. KS model

To demonstrate the robustness of our theory we also compare its predictions to results of numerical simulations using a different model for the turbulent flow, namely the KS model [54]. The KS model has been shown to reproduce qualitatively many features of turbulent transport, and it provides a convenient way to represent a flow with a wide range of spatial scales, such as turbulence, albeit in a simplified manner. In short, we discretise Fourier space in geometrically spaced shells, up to a largest wavenumber. The largest and smallest length scales of the flow are L and η, respectively. The total number of shells is denoted by N_k. We choose the characteristic wave vector in shell n as: $k_n = k_1(L/\eta)^{(n-1)/(N_k-1)}$. In each cell, we pick one wave vector, $\boldsymbol{k}_n$. The flow is then simply constructed as a sum of Fourier modes:

$$\boldsymbol{u}(\boldsymbol{x}, t) = \sum_{n=1}^{N_k} \boldsymbol{a}_n \cos(\boldsymbol{k}_n \cdot \boldsymbol{x} + \omega_n t) + \boldsymbol{b}_n \sin(\boldsymbol{k}_n \cdot \boldsymbol{x} + \omega_n t). \tag{23}$$

The Fourier coefficients are chosen so that $\boldsymbol{k}_n \cdot \mathbf{a}_n = \boldsymbol{k}_n \cdot \boldsymbol{b}_n = 0$ (incompressibility), and with magnitude $a_n^2 = b_n^2 = E(k_n)\Delta k_n$, where $E(k_n) = E_0 k_n^{-5/3}$ represents the Kolmogorov spectrum [58]. The frequency ω_n in equation (23) is taken to be $\omega_n = \frac{1}{2}\sqrt{k_n^3 E(k_n)}$. Further details about the implementation of this model for $\boldsymbol{u}(\boldsymbol{x}, t)$ can be found in [55].

3. Orientation distributions

Figure 2 shows orientation distributions obtained by numerical simulations of equations (14) for the three-dimensional statistical model described in section 2.2. Shown are distributions of $n_g = \boldsymbol{n} \cdot \hat{\boldsymbol{g}}$ for rod-like particles with aspect ratio $\lambda = 5$, for different Stokes and settling numbers. We see that the particles settle with their broadside approximately aligned with gravity, that is $n_g \approx 0$. This is the stable orientation for prolate particles settling in a quiescent fluid [25, 26].

Compare the distributions in figure 2 to those shown in [48]. Figure 1(b) of [48] corresponds to rods that tend to settle tip first. The reason for the difference is that the effect of the fluid-inertia torque was neglected in [48], whereas in the present work we choose parameters where this torque dominates the angular dynamics.

When the Stokes number is small we expect that the vector $\boldsymbol{n}$ spends most of its time close to a stable fixed point of the angular dynamics. As mentioned above, this fixed point is $n_g = 0$ in the absence of turbulence. But the turbulent velocity gradients must modify this fixed point. How does this affect the orientations of the settling particles? Figure 2 shows that the orientation distribution is still peaked at $n_g = 0$, but that it acquires a finite width. The question is how the width depends upon the parameters of the problem, on the settling number Sv and upon the Stokes number St. Figure 2 indicates that the width decreases as Sv increases at fixed St, and that the width increases as the Stokes number St increases at fixed Sv. In the following we first consider small Stokes numbers, because the problem simplifies in this overdamped limit. In this limit we expect that the particle orientation follows the fixed-point orientation quite closely. This allows us to derive a theory for the orientation distribution in this limit, described in the following section.

4. Overdamped limit

Assume that the relaxation time of $\boldsymbol{n}$ is much faster than the time scale on which the gradients change as the particle moves through the flow. This corresponds to the overdamped limit of the problem, $\mathrm{St} \to 0$ in equations (14). It was shown by experiments and numerical simulations in [51] that this limit quantitatively describes the orientation distribution of rods settling in a 2D vortex flow, and in the slender-body limit this approach was also used in [56, 69].

We also assume that Sv is large enough so that the fluid-inertia torque dominates the angular dynamics. This allows us to take into account turbulent fluctuations perturbatively. It also means that we can approximate the instantaneous slip velocity by $\boldsymbol{W}^{(0)}(\boldsymbol{n})$, equation (6). In this limit we find:

$$\boldsymbol{W} = \boldsymbol{W}^{(0)}(\boldsymbol{n}), \tag{24a}$$

$$\boldsymbol{\omega}_\mathrm{p} = \boldsymbol{\Omega} + \Lambda(\boldsymbol{n} \wedge \mathbb{S}\boldsymbol{n}) + \mathscr{A}\mathrm{Sv}^2 n_g(\boldsymbol{n} \wedge \hat{\boldsymbol{g}}), \tag{24b}$$

with $n_g = \boldsymbol{n} \cdot \hat{\boldsymbol{g}}$, as defined in section 3. The overdamped equation for the dynamics of the vector $\boldsymbol{n}$ corresponding to equation (24*b*) reads

$$\dot{\boldsymbol{n}} = \mathbb{O}\boldsymbol{n} + \Lambda[\mathbb{S}\boldsymbol{n} - (\boldsymbol{n} \cdot \mathbb{S}\boldsymbol{n})\boldsymbol{n}] + \mathscr{A}\mathrm{Sv}^2 n_g(\hat{\boldsymbol{g}} - n_g\boldsymbol{n}). \tag{24c}$$

To simplify the notation we introduced the parameter

$$\mathscr{A} = \mathscr{A}'\frac{I_\perp}{A_\parallel A_\perp C_\perp}. \tag{25}$$

Figure 1(b) shows how $\mathscr{A}$ depends on the particle-aspect ratio λ.

4.1. Two-dimensional dynamics in the overdamped limit

We consider the 2D model first because it is much easier to analyse than the three-dimensional model. We assume that the gravitational acceleration points into the $\hat{\mathbf{e}}_1$-direction, and define ϕ to be the angle ($0 \leqslant \phi < \pi$) between $\boldsymbol{n}$ and this axis, so that $n_g = \boldsymbol{n} \cdot \hat{\boldsymbol{g}} = \cos\phi$. For prolate particles ($\lambda > 1$ or equivalently $\Lambda > 0$) the overdamped angular dynamics (24*c*) becomes in two spatial dimensions:

$$\frac{\mathrm{d}}{\mathrm{d}t}\phi = -O_{12} + \Lambda[S_{12}\cos(2\phi) - S_{11}\sin(2\phi)] + \tfrac{1}{2}|\mathscr{A}|\,\mathrm{Sv}^2\sin(2\phi). \tag{26}$$

This 2D overdamped equation of motion for the angular dynamics is essentially equivalent to model M2 in [51], used there for simulations of the angular dynamics of rods settling in a 2D vortex flow. Apart from the fact that [51] considers a different flow, it describes small cylindrical particles with slightly different resistance tensors, and it approximates the $\boldsymbol{n}$-dependence of the settling velocity. Equation (26) shows that the fluid-inertia torque has the same angular dependence as the S_{11}-component of the strain, but in general the sign may differ. When $S_{11} > 0$, the strain tends to align the rod with $\hat{\mathbf{e}}_1$, the direction of gravity. The fluid-inertia torque acts against alignment with this direction. To quantify this statement, consider the fixed points of the angular dynamics (26). In the limit $|\mathscr{A}|\mathrm{Sv}^2 \to \infty$, the inertial torque dominates the angular dynamics, so that the fluid-velocity gradients do not matter. In this limit the fixed points are $\phi_1^* = 0$ and $\phi_2^* = \pi/2$. For a prolate particle ($\lambda > 1$) $\phi_1^* = 0$ is unstable while $\phi_2^* = \pi/2$ is stable. This is the limit considered in [25], a slender rod falling in a quiescent fluid: since ϕ_2^* is stable the rod settles with its broad side first. The same is true more generally for prolate axisymmetric particles settling in a quiescent fluid [26].

Now, what is the effect of the turbulent flow? In general this question is difficult to answer. But if the angle ϕ relaxes much faster than the fluid-velocity gradients change along the particle path, then the problem becomes tractable. Assuming that the gradients are constant, we can find exact expressions for the two fixed points of equation (26), for arbitrary aspect ratios and fluid-velocity gradients. We take $\lambda > 1$ and expand the stable fixed point around $\pi/2$ assuming that $|\mathscr{A}|\mathrm{Sv}^2$ is large:

$$\phi_2^* = \frac{\pi}{2} - B_{12}\frac{1}{|\mathscr{A}|\mathrm{Sv}^2} - 2B_{11}B_{12}\frac{1}{(\mathscr{A}\mathrm{Sv}^2)^2} + \ldots \tag{27}$$

Here B_{ij} are the elements of the matrix $\mathbb{B} = \mathbb{O} + \Lambda\mathbb{S}$. Equation (27) shows how the fixed-point orientation $\phi_2^*(t)$ changes as a function of $\mathbb{B}(t)$, as the turbulent velocity gradients evolve. We expect that the orientation of a settling rod follows the fixed-point orientation $\phi_2^*(t)$ quite closely in the overdamped limit, provided that its angular relaxation time is smaller than the time scale on which the flow (and thus ϕ_2^*) changes.

Figure 3 shows examples of how the fixed point $\phi_2^*(t)$ of the angular dynamics fluctuates as the particle settles through the turbulent flow and encounters different fluid-velocity gradients. The data are obtained by numerical simulation of the 2D model described in section 2, for small Stokes numbers. Also shown is the instantaneous angle $\phi(t)$ obtained in these simulations. We see that the orientation dynamics follows the fixed point ϕ_2^* quite closely when St is small. In this case the orientation distribution of the settling particle is determined by the distribution of

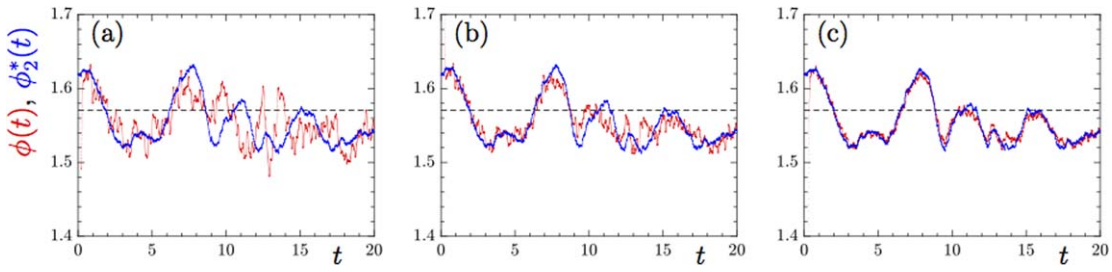

Figure 3. Angular dynamics of a settling particle in two spatial dimensions. Shown is the angle $\phi(t)$ obtained by simulation of equation (14) (red), and the analytically exact result for the stable fixed point $\phi_2^*(t)$ (blue). (a) St $= 0.1$, (b) St $= 0.05$, (c) St $= 0.02$. Other parameters: Sv $= 25$, $\lambda = 5$. The three simulations were performed with the same initial conditions and for the same realisation of the function $\boldsymbol{u}(\boldsymbol{x}, t)$ in the 2D statistical model.

ϕ_2^*, and thus by the distribution of fluid-velocity gradients encountered by the particle, through equation (27). This distribution may differ from the distribution of fluid-velocity gradients at a fixed spatial position (preferential sampling [53]). But in the overdamped limit preferential sampling of the fluid-velocity gradients is expected to be weak for settling particles. We have checked that it is negligible for data shown in this paper.

If we consider only the leading correction in equation (27), then the orientation distribution is determined by the distribution $P_B(B_{12})$ of B_{12}:

$$P(\phi) = \int_{-\infty}^{\infty} \mathrm{d}B_{12}\, P_B(B_{12})\, \delta\left(\phi - \frac{\pi}{2} + \frac{B_{12}}{|\mathscr{A}|\mathrm{Sv}^2}\right) = P_B\left[\left(\tfrac{\pi}{2} - \phi\right)|\mathscr{A}|\mathrm{Sv}^2\right]. \tag{28}$$

In the 2D statistical model the distribution $P_B(B_{12})$ is Gaussian with variance $\sigma_B^2 = \frac{1}{8}(2 + \Lambda^2)$. This means that the distribution of ϕ is Gaussian too:

$$P(\phi) = \frac{\mathrm{e}^{-\frac{(\phi-\pi/2)^2}{2\sigma_\phi^2}}}{\sqrt{2\pi\sigma_\phi^2}}, \tag{29}$$

with variance

$$\sigma_\phi^2 = \frac{1}{8}\frac{2 + \Lambda^2}{(|\mathscr{A}|\mathrm{Sv}^2)^2}. \tag{30}$$

Equation (28) shows that the distribution of ϕ simply reflects the magnitude of the fluctuations of the fluid-velocity gradients, at least when the particle orientation relaxes faster than the fluid-velocity gradients change (see below for a full discussion). The corresponding distribution of $n_g = \boldsymbol{n} \cdot \hat{\boldsymbol{g}}$ is:

$$P(n_g) = \frac{1}{\sin\phi} P(\phi) = \frac{\exp[-(\mathrm{acos}(n_g) - \pi/2)^2/(2\sigma_\phi^2)]}{\sqrt{2\pi\sigma_\phi^2}\sqrt{1 - n_g^2}}. \tag{31}$$

Figure 4 shows that equations (29) and (30) agree well with results of simulations of the overdamped dynamics in two spatial dimensions, provided that St is small enough (panel (a)). In this case the orientation variance decreases as Sv^{-4} as Sv increases.

The model predicts that the orientation distribution broadens as the particle aspect ratio λ increases (full lines). This is consistent with the numerical results (symbols), and can be readily explained by noticing that $|\mathscr{A}|$ is a decreasing function of λ, see figure 1(b). As a consequence, the variance of the fluctuations, $\propto 1/\mathscr{A}^2$, increases as λ grows. When the Stokes number becomes larger [panel (b)], the distribution is much wider than predicted by the overdamped theory.

The theory outlined above assumes that the angular dynamics (26) responds so rapidly that the orientation of the particle follows the instantaneous fixed point of the dynamical system (26) quite closely. To quantify more precisely when this theory applies we must consider the relaxation time τ_ϕ of the angular dynamics. In units of τ_K it is given by the inverse of the stability exponent σ of the fixed point ϕ_2^*. In keeping with the assumptions underlying equation (27) we require

$$|\mathscr{A}|\mathrm{Sv}^2 \gg 1. \tag{32}$$

First, to leading order in $(|\mathscr{A}|\mathrm{Sv}^2)^{-1}$ we find from equation (26) that $\sigma \sim -|\mathscr{A}|\mathrm{Sv}^2$. This gives

$$\tau_\phi \sim |\sigma^{-1}| = \frac{1}{|\mathscr{A}|\mathrm{Sv}^2}, \tag{33}$$

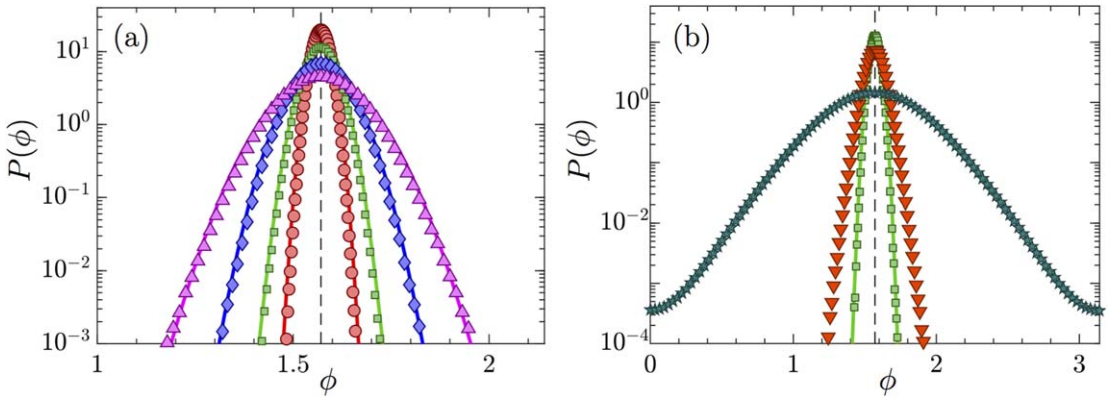

Figure 4. Orientation distributions for the two-dimensional statistical model. (a) Distribution of angle $\phi = \mathrm{acos}(n_g)$ obtained from numerical simulation of the dynamics (14) (markers) and the limiting theory for small Stokes numbers, equation (29) (solid lines). Parameters: Sv = 22, St = 0.022, and $\lambda = 3$ (red, ∘), $\lambda = 5$ (green, □), $\lambda = 7.5$ (blue, ◊), $\lambda = 10$ (magenta, △). (b) Same, but for different Stokes numbers. Parameters: $\lambda = 5$, and St = 0.022 (green, □), St = 0.22 (red, ▽), St = 22 (dark green, ⋆).

and equation (32) implies that $\tau_\phi \ll 1$. Second, when Sv is large, the fluid-velocity gradients seen by the settling particle change at the settling time scale τ_s, the time it takes a particle settling with an angle $\phi = \pi/2$ at a settling velocity given by equation (6) to fall one correlation length ℓ

$$\tau_\mathrm{s} = \frac{1}{\tau_\mathrm{K}}\frac{\ell A_\perp}{\tau_\mathrm{p} g} = \frac{\ell}{\eta_\mathrm{K}}\frac{A_\perp}{\mathrm{Sv}}. \tag{34}$$

We therefore conclude that the theory outlined above holds if

$$\frac{\tau_\phi}{\tau_\mathrm{s}} = \frac{1}{A_\perp |\mathscr{A}|\mathrm{Sv}}\frac{\eta_\mathrm{K}}{\ell} \ll 1. \tag{35}$$

This condition ensures that the gradient dynamics is 'persistent' [70], in the sense that the fluid-velocity gradients change much more slowly than the angular particle dynamics relaxes. Equation (35) indicates that the persistent limit is achieved provided that $|\mathscr{A}|\mathrm{Sv}$ is large enough, at least for the overdamped dynamics (26). For smaller values of Sv the overdamped theory is modified in at least two ways. First, the fixed point (27) may annihilate in a bifurcation with ϕ_1^*. Likewise, the time scale τ_ϕ may depend on the instantaneous fluid-velocity gradients if the condition (32) does not hold. Second, the time scale at which the particle samples the fluid-velocity gradients is different: at small Sv this time scale is no longer τ_s. Instead the Kolmogorov time τ_K must be used in equation (35). Here we do not discuss this limit further. The results derived above, and in the remainder of this paper, assume that the condition (32) is satisfied.

4.2. Three-dimensional dynamics in the overdamped limit

In this section we show how to obtain the distribution of $n_g = \boldsymbol{n}\cdot\hat{\boldsymbol{g}}$ for the three-dimensional statistical model, in the same overdamped and persistent limit considered above. The calculation is analogous to the one described in section 4.1. Let $\boldsymbol{p} = \boldsymbol{n} - n_g\hat{\boldsymbol{g}}$. Using $p^2 = 1 - n_g^2$ we express the equation of motion (24c) of n_g as

$$\begin{aligned}\dot{n}_g &= \hat{\boldsymbol{g}}\cdot\dot{\boldsymbol{n}} = \hat{\boldsymbol{g}}\cdot\mathbb{O}\boldsymbol{n} + \Lambda[\hat{\boldsymbol{g}}\cdot\mathbb{S}\boldsymbol{n} - (\boldsymbol{n}\cdot\mathbb{S}\boldsymbol{n})n_g] + \mathscr{A}\mathrm{Sv}^2 n_g(1-n_g^2)\\ &= O_{gp} + \Lambda[(1-2n_g^2)S_{gp} + n_g(1-n_g^2)S_{gg} - n_g S_{pp}] + \mathscr{A}\mathrm{Sv}^2 n_g(1-n_g^2).\end{aligned} \tag{36}$$

Here the subscripts g and p denote contractions with $\hat{\boldsymbol{g}}$ and $\boldsymbol{p}$. In the limit of $|\mathscr{A}|\mathrm{Sv}^2 \to \infty$, $n_g^* = 0$ is the stable fixed point for prolate particles ($\lambda > 1$). To determine how the fixed point changes due to fluid-velocity fluctuations we seek an expansion in $(|\mathscr{A}|\mathrm{Sv}^2)^{-1}$ as in section 4.1, of the form $n_g^* \propto 1/(|\mathscr{A}|\mathrm{Sv}^2) + \ldots$. We obtain to leading order:

$$n_g^* = \frac{\hat{\boldsymbol{g}}\cdot\mathbb{B}\boldsymbol{p}}{|\mathscr{A}|\mathrm{Sv}^2}. \tag{37}$$

Assuming that the orientation of $\boldsymbol{p}$ is uncorrelated from the fluid-velocity gradients, we obtain for the variance of the distribution of n_g:

$$\sigma_{n_g}^2 = \frac{\langle B_{12}^2\rangle\langle|\boldsymbol{p}|^2\rangle}{(|\mathscr{A}|\mathrm{Sv}^2)^2} \approx \frac{\sigma_B^2}{(|\mathscr{A}|\mathrm{Sv}^2)^2}, \tag{38}$$

where σ_B^2 is the variance of the distribution of B_{12} (the gravitational acceleration points in the $\hat{\mathbf{e}}_1$-direction). We also used that $p^2 = 1 - n_g^2 \approx 1$. This is a good approximation because in the limit we consider n_g is small for prolate particles. Assuming that $\boldsymbol{p}$ and the fluid-velocity gradients are uncorrelated implies that the distribution

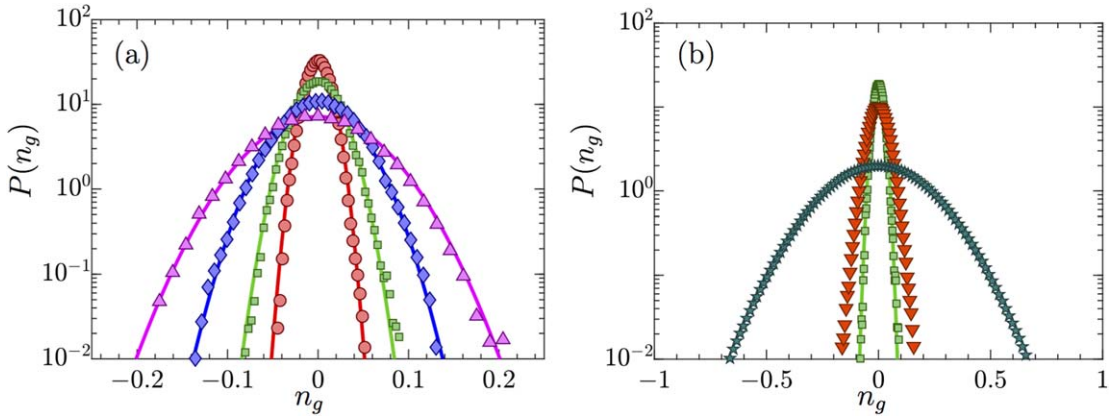

Figure 5. Orientation distribution for the three-dimensional statistical model. Same conventions and parameters as in figure 4. (a) $P(n_g)$ in the overdamped limit. (b) Same, but for different Stokes numbers.

of n_g is Gaussian in the statistical model:

$$P(n_g) = \frac{1}{\sqrt{2\pi}\,\sigma_{n_g}} \exp\left(-\frac{n_g^2}{2\sigma_{n_g}^2}\right), \tag{39}$$

and the variance evaluates to

$$\sigma_{n_g}^2 = \frac{1}{(|\mathscr{A}|\mathrm{Sv}^2)^2}\frac{5+3\Lambda^2}{60}. \tag{40}$$

Figure 5 shows results for the distribution of n_g from simulations of the three-dimensional statistical model. Panel (a) shows results for small Stokes numbers, the parameters are the same as in figure 4(a). Also shown are the results of the theory, equations (39) and (40). In this case St is small enough and Sv large enough so that the theory works very well. Panel (b) shows the orientation distribution for different Stokes numbers, to demonstrate how the theory fails when the Stokes number becomes larger. The behaviour is similar to that described in section 4.1: the distribution widens as St increases.

Equation (38) says that the variance of the distribution of n_g is inversely proportional to the fourth power of Sv, $\sigma_{n_g}^2 \propto \mathrm{Sv}^{-4}$, for large values of the settling number provided that the Stokes number is small enough. In figure 6(a) this prediction is compared with results of simulations of the three-dimensional statistical model. Shown is the variance of n_g as a function of Sv, for two Stokes numbers. When the Stokes number is small we see that the prediction (40) works well for large Sv, as expected. Figure 6(b) shows the kurtosis $\beta_2 = \langle n_g^4\rangle / \langle n_g^2\rangle^2$, measuring the flatness of the distribution $P(n_g)$. As predicted by the theory, the kurtosis approaches the Gaussian limit ($\beta_2 = 3$) for large settling numbers, at small enough Stokes numbers.

When $\mathrm{Sv} \to 0$ the variance tends to $\frac{1}{3}$ and $\beta_2 \to \frac{9}{5}$, indicating that equation (40) fails because condition (32) is no longer satisfied. In this limit the distribution of n_g becomes uniform and independent of the Stokes number, because the angular dynamics is isotropic when gravitational settling is weak. Figure 6(c) shows results for the variance from numerical simulations using the KS model (section 2.3), for three different values of the Stokes number. The results are very similar to those obtained using the statistical model (figure 6(a)). There is good agreement with the overdamped theory, equation (38), at large Sv for small enough St. We determined σ_B^2 from the KS simulations, so there are no fitting parameters in figure 6(c). The good agreement shows that the overdamped theory is robust, insensitive to the details of the spectrum of the velocity fluctuations. Figure 6 also shows numerical data for larger values of St. For small Sv this makes little difference, the distribution is uniform. For larger Sv the numerical results first follow equation (38) or (40). But as Sv increases further, the overdamped theory starts to fail, the earlier the larger the Stokes number. This indicates that particle inertia begins to become important.

The results obtained here rely on the statistical model described in section 2.2, based on a simplified model for the turbulent fluid velocity-gradients. In turbulence there are subtle correlations between vorticity and strain that are essential for the alignment between the rod direction and vorticity [30], in the absence of settling, and in the overdamped limit. These correlations are neglected in the statistical model, but we argue that the results presented here are insensitive to these correlations. The alignment between orientation and vorticity builds up over a time scale of the order of a few τ_K [71] (see also figure 1 of [30]). Since heavy settling particles do not follow the motion of fluid particles, the correlations between vorticity and strain do not play a significant role, in

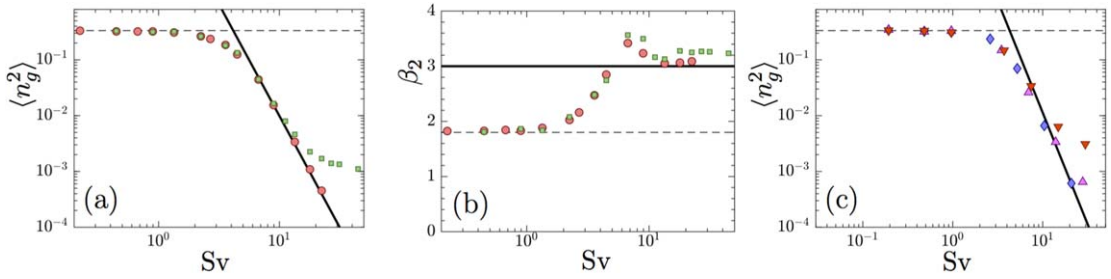

Figure 6. Width of the orientation distribution. (a) Variance of n_g from simulations of the three-dimensional model, as a function of Sv, for two values of the Stokes number: St $= 0.022$ (red, ∘) and St $= 0.22$ (green, □). Also shown is the theory for large Sv, equation (40), solid line, and the result for a uniform distribution, $\langle n_g^2\rangle = \frac{1}{3}$ (dashed line). (b) Kurtosis $\beta_2 = \langle n_g^4\rangle / \langle n_g^2\rangle^2$. Same parameters as in panel (a). The overdamped theory (section 4.2) gives a Gaussian distribution with kurtosis equal to $\beta_2 = 3$ (solid line). For a uniform distribution, $\beta_2 = \frac{9}{5}$ (dashed line). (c) Results for $\sigma^2_{n_g}$ from KS for St $= 0.025$ (blue, ◇), 0.1 (magenta, △), and 0.4 (red, ▽). Also shown is the theory, equation (38), solid line, as well as the uniform limit (dashed line).

particular for large Sv. This is consistent with comparisons between the results of DNS and of the statistical model in [48], showing quantitative agreement between the two approaches.

Finally we remark that the orientation distributions (29) and (39) are Gaussian in the statistical model. This follows from the simplifying assumption that the velocity-gradient statistics is Gaussian. In turbulence this is not the case, as explained in section 2.2. The overdamped theory shows that the angular distribution simply mirrors any non-Gaussian features of the turbulence velocity-gradient statistics, equation (28). Similarly, the relation (38) between the orientation variance and the variance σ_B^2 holds also for turbulence—where the corresponding distributions are not Gaussian.

5. Beyond the overdamped limit

The overdamped theory in the previous section was derived for large Sv. Panels (a) and (c) of figure 6 show that this theory describes the numerical results very well. However, the figure also exhibits deviations from the theory at very large values of Sv when the Stokes number is small, but finite. To understand when and why the overdamped theory fails one must check the full inertial dynamics. To this end we begin by analysing the 2D statistical model.

5.1. Two-dimensional model

To estimate the time scales that are important for the inertial angular dynamics, we consider the limit where the torque due to fluid inertia dominates over Jeffery's torque, as in the previous section. In the overdamped limit this led to condition (32). For a qualitative analysis of the inertial angular dynamics we not only set the fluid-velocity gradients to zero, $\mathbb{A} = 0$, but also the fluid velocity, $\boldsymbol{u} = 0$. In this case the dynamics of the phase-space coordinate $\boldsymbol{z} \equiv (v_{px}, v_{py}, \phi, \omega_p)$ has the stable fixed point $\boldsymbol{z}^* = (\mathrm{Sv}/A_\perp, 0, \pi/2, 0)$, where gravity points in the direction of $\hat{\mathbf{e}}_1$. The stability matrix follows from equation (14):

$$\mathbb{J} \equiv \frac{\partial \dot{\boldsymbol{z}}}{\partial \boldsymbol{z}} = \frac{1}{\mathrm{St}} \begin{bmatrix} -A_\perp & 0 & 0 & 0 \\ 0 & -A_\parallel & \dfrac{A_\parallel - A_\perp}{A_\perp}\mathrm{Sv} & 0 \\ 0 & 0 & 0 & \mathrm{St} \\ 0 & -\dfrac{\mathscr{A}'}{A_\perp}\mathrm{Sv} & +\dfrac{\mathscr{A}'}{A_\perp^2}\mathrm{Sv}^2 & -\dfrac{C_\perp}{I_\perp} \end{bmatrix}, \tag{41}$$

where $\mathscr{A}'$ was defined in equation (17). The relaxation time following from equation (41) is given by $\tau_\phi = \max(-1/\Re\sigma_i)$, the maximal stability time of J. Here $\Re\sigma_i$ denotes the real part of the i^{th} eigenvalue of $\mathbb{J}$. One eigenvalue of this matrix is $\sigma = -A_\perp/\mathrm{St}$. We have computed the other eigenvalues numerically and analytically in limiting cases. We find that the time scale τ_ϕ interpolates between equation (33) for small St and $\sim \mathrm{St}/A_\perp$ for large St, for a fixed value of Sv. If we fix St, by contrast, then we find that the time scale τ_ϕ interpolates between equation (33) for small Sv and $\sim \mathrm{St}/A_\perp$ for large Sv. We remark, however, that if Sv is not large enough, then one cannot justify to neglect the fluid-velocity gradients in the stability matrix (41), so that any argument based on equation (41) must break down.

We expect that the overdamped approximation fails when the inertial estimate for the relaxation time of the angular dynamics, $\tau_\phi \sim \mathrm{St}/A_\perp$, becomes larger than the overdamped estimate equation (33). This means that the

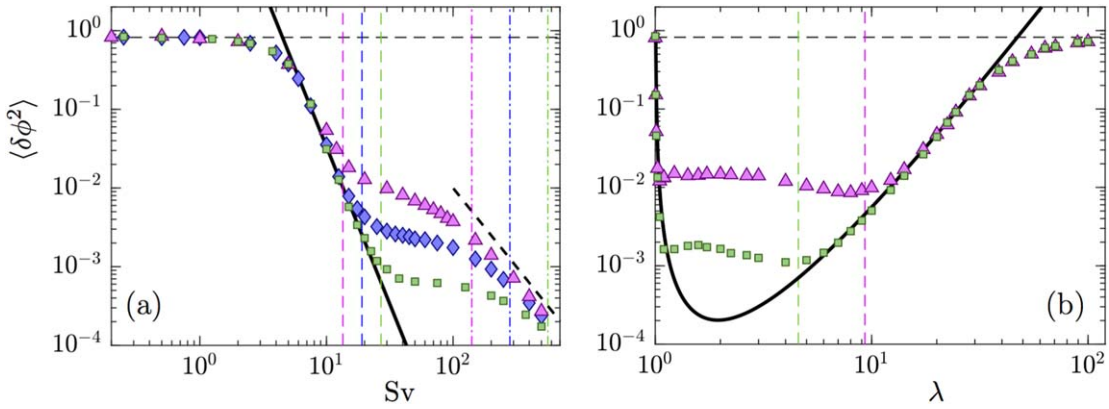

Figure 7. Variance $\langle\delta\phi^2\rangle$ for the two-dimensional statistical model. (a) Results of numerical simulations as a function of Sv for $\lambda = 5$, St $= 0.1$ (green, □), St $= 0.2$ (blue, ◇), St $= 0.4$, (magenta, △). Also shown: theory from section 4.1, equations (29) and (30), thick solid black line; condition $|\mathscr{A}|\mathrm{Sv}^2 = A_\perp/\mathrm{St}$ for the overdamped theory to fail [equation (42)], vertical dashed lines; condition (44) for the white-noise limit, vertical dashed–dotted lines; large-Sv scaling (43), thick black dashed line; uniform distribution at small Sv, horizontal black dashed line. (b) Results as a function of the particle aspect ratio λ for Sv $= 25$, St $= 0.1$ (green, □), and St $= 0.4$ (magenta, △).

overdamped approximation requires

$$|\mathscr{A}|\mathrm{Sv}^2 \ll A_\perp/\mathrm{St}. \tag{42}$$

Conversely, when equation (42) is not satisfied then particle inertia matters, so that the overdamped approximation must fail (figure 6(a)). For a quantitative comparison, figure 7(a) shows numerical results for the variance of the orientation distribution obtained from simulations of the 2D model. We see that the overdamped approximation breaks down for values of Sv larger than $\sim\sqrt{A_\perp/(|\mathscr{A}|\mathrm{St})}$, as predicted by equation (42). We observe that the variance decreases more slowly as Sv increases further.

Figure 7(a) also reveals that there is yet another, asymptotic regime at very large values of Sv—so large that it is difficult to achieve small Re_p at the same time. It is nevertheless of interest to analyse this regime, because it reveals the ingredients that a theory describing effects of particle inertia must contain. Figure 7(a) suggests that

$$\langle n_g^2\rangle \sim \frac{c_1}{\mathrm{Sv}^2} \tag{43}$$

for very large values of Sv. Our simulations indicate that the prefactor c_1 depends upon ℓ/η_K, St, and upon λ (not shown). We surmise that this regime describes particles settling so rapidly that the settling time scale τ_s is the smallest time scale in the system. This cannot hold unless $\tau_\phi \sim \mathrm{St}/A_\perp$ is much larger than τ_s, and this crossover occurs at

$$\frac{\mathrm{Sv}\,\mathrm{St}}{A_\perp^2}\frac{\eta_\mathrm{K}}{\ell} \sim 1. \tag{44}$$

We expect equation (43) to be accurate for values of Sv much larger than those given by equation (44). This condition is also shown in figure 7, and we see that the large-Sv regime starts at values of Sv approximately satisfying (44). Since condition (42) is violated in this regime, particle inertia must be taken into account. A difficulty is that particle inertia changes the translational as well as the angular dynamics. Thus it is no longer guaranteed that $\boldsymbol{W} = \boldsymbol{W}^{(0)}(\boldsymbol{n})$ (assumed in the overdamped theory of section 4). This means that particle inertia is expected to modify the angular dynamics in at least two ways. Firstly, it introduces the time derivative $\frac{\mathrm{d}^2}{\mathrm{d}t^2}\delta\phi$ into the angular dynamics. Secondly, the fluctuations of the torque change because $\boldsymbol{W} \neq \boldsymbol{W}^{(0)}(\boldsymbol{n})$ when particle inertia matters. This is discussed in section 5.2.

Figure 7(b) shows how the variance of $\delta\phi$ depends on particle shape, for fixed Sv and St. There are four regimes. First, in the limit $\lambda \to \infty$ the distribution is uniform and independent of the Stokes number. In this regime the dynamics is overdamped (condition (42)), but the persistent approximation fails because equation (32) is not satisfied. Second, for intermediate aspect ratios, both conditions are satisfied, so that the theory (equations (29) and (30)) is accurate. Third, as λ becomes smaller, the overdamped approximation breaks down. In this regime particle inertia must be taken into account. Fourth, as $\lambda \to 1$ the orientation distribution must become uniform. This cross-over happens very rapidly: for spheres ($\lambda = 1$) the orientation distribution is uniform, but already for $\lambda \sim 1.05$ there is strong alignment.

We conclude this section with a remark concerning figure 7(b): the overdamped theory (30) predicts that the variance of $\delta\phi$ grows as the aspect ratio λ increases, provided that St and Sv are kept constant. In physical terms this is a consequence of the fact that the mobility coefficients become smaller as λ increases. A smaller

translational mobility ($A_\parallel^{-1}$ and $A_\perp^{-1}$) reduces the magnitude of the slip velocity in equation (14*d*), while smaller rotational mobility $I_\perp C_\perp^{-1}$ increases the effect of the fluid-velocity gradients upon the angular dynamics of the particle. Both tendencies diminish the effect of the fluid-inertia torque in equation (14*d*) as λ grows, diminishing its tendency to align the particles. This prediction is in good agreement with the 2D simulation results shown in figure 7(b).

5.2. Klett's small-angle expansion

Klett [28] proposed a theory for the orientation variance of nearly spherical particles settling in turbulence, including particle inertia in the angular dynamics. He uses that the orientation variance is very small for large values of Sv. This suggests to expand the equations of motion in small deviations of the angle $\phi = \mathrm{acos}(\boldsymbol{n}\cdot\hat{\boldsymbol{g}})$ from its equilibrium value: $\phi = \phi^* + \delta\phi$ where $\phi^* = \frac{\pi}{2}$ for prolate particles. Klett assumes that $\boldsymbol{W} = \boldsymbol{W}^{(0)}(\boldsymbol{n})$ (equation (6)) and expands the angular dynamics for nearly spherical particles in $\delta\phi$.

We can derive an equation of motion consistent with his by expanding equations (14) to leading order in $\delta\phi$, assuming that $\boldsymbol{W} = \boldsymbol{W}^{(0)}(\boldsymbol{n})$, retaining only the leading terms in $(|\mathscr{A}|\mathrm{Sv}^2)^{-1}$ (we must also require that St is small, in keeping with Klett's assumptions). In this way we obtain for a prolate particle of arbitrary aspect ratio in three spatial dimensions:

$$\frac{\mathrm{d}^2}{\mathrm{d}t^2}\delta\phi + \frac{C_\perp}{I_\perp\,\mathrm{St}}\frac{\mathrm{d}}{\mathrm{d}t}\delta\phi + \frac{C_\perp}{I_\perp\,\mathrm{St}}|\mathscr{A}|\mathrm{Sv}^2\delta\phi = -\frac{C_\perp}{I_\perp\,\mathrm{St}}\,\hat{\boldsymbol{g}}\cdot\mathbb{B}\boldsymbol{p}. \tag{45}$$

When we expand the geometrical coefficients in equation (45) for small Λ we find that the prefactors of the terms on the lhs of this equation are almost identical, in this limit, to those in equation (17) of [28]. Slight discrepancies arise in the $\delta\phi$-term because we use the expression for the inertial torque from [26], while Klett uses the form obtained by Cox [24] (the relative error of the prefactors is of the order of 10^{-3} [26]). At any rate, equation (45) is simply a damped driven harmonic oscillator, with implicit solution

$$\delta\phi(t) = \frac{C_\perp}{\Omega_0 I_\perp\,\mathrm{St}}\int_0^t \mathrm{d}t_1\,\mathrm{e}^{C_\perp(t_1-t)/(2I_\perp\mathrm{St})}\sin[\Omega_0(t_1-t)]\,\hat{\boldsymbol{g}}\cdot\mathbb{B}(t_1)\boldsymbol{p}. \tag{46}$$

Here $\Omega_0 = [C_\perp/(2I_\perp\mathrm{St})]\sqrt{4|\mathscr{A}|\mathrm{Sv}^2 I_\perp\,\mathrm{St}/C_\perp - 1}$. Note that we discarded terms related to the initial angle, because they cannot be important for the steady-state variance of $\delta\phi$ in the limit of large Sv, at fixed St. Squaring equation (46) and averaging over realisations of the turbulent fluctuations in the statistical model we obtain for large Sv

$$\langle\delta\phi^2\rangle \sim \frac{c_0}{\mathrm{Sv}^4}, \tag{47}$$

where c_0 is a function of ℓ/η_K, St, and of the aspect ratio λ. We neglected a Sv^{-3} contribution to $\langle\delta\phi^2\rangle$ because it is exponentially suppressed. Equation (47) fails to describe the large-Sv behaviour (43), shown as the thick black dashed line in figure 7. This means that equation (45) cannot be used to estimate the large-Sv width of the orientation distribution, or to compute deviations from the overdamped theory.

Which approximation causes equation (45) to fail? Since the variance is small for large Sv, $\delta\phi$ remains small at all times. Therefore we see no reason to doubt that the small-angle expansion is valid. This leads us to conclude that the assumption $\boldsymbol{W} = \boldsymbol{W}^{(0)}(\boldsymbol{n})$ breaks down, in agreement with our conclusions in the previous section. To check this, we artificially imposed the constraint $\boldsymbol{W} = \boldsymbol{W}^{(0)}(\boldsymbol{n})$ in simulations of the 2D statistical model. The resulting large-Sv variance follows equation (47), and thus fails to give the correct scaling, equation (43). This demonstrates that it is important to allow $\boldsymbol{W}$ to deviate from $\boldsymbol{W}^{(0)}(\boldsymbol{n})$ when particle inertia matters.

Klett obtains that $\langle\delta\phi^2\rangle \propto \mathrm{Sv}^{-2}$, assuming that the fluid-velocity gradients on the right-hand side of equation (45) are just white noise in time. This scaling is consistent with the large-Sv power law observed in Figure 7 (a), but Klett's theory is difficult to justify from first principles because it neglects fluctuations of $\boldsymbol{W} - \boldsymbol{W}^{(0)}(\boldsymbol{n}_t)$ that yield additional time-dependent terms in the angular equation of motion (45), which are expected to affect the prefactor of the Sv^{-2} scaling. More importantly, the 2D simulation results shown in figure 7 demonstrate that $\langle\delta\phi^2\rangle \propto \mathrm{Sv}^{-2}$ applies only in the unphysical limit of very large Sv, and that particle inertia causes a complex parameter dependence of the orientation variance at smaller values of Sv, with a number of different regimes to consider.

6. Conclusions

Convective fluid inertia affects the orientation of a small axisymmetric particle settling in a turbulent flow. In [5, 6, 47–49] this effect was neglected. Here we considered a limit of the problem where it is dominant, but where turbulent fluctuations still matter. This limit is relevant to computing the distribution of orientation of ice crystals settling in turbulent clouds [1]. Our goal was to compute the distribution of orientations of a spheroid in turbulence, to work out how the torques due to convective fluid inertia and due to the turbulent velocity

gradients affect the orientation distribution. In general the angular dynamics of the settling particle is very complicated. Here we looked at a limit in which the problem becomes tractable: we assumed small Stokes number (a dimensionless measure of particle inertia) and large settling number (dimensionless settling speed). For small Stokes numbers the dynamics is overdamped. For large values of the settling number, the problem becomes persistent: the angular dynamics relaxes much faster than the fluid-velocity gradients change. In this limit the angular dynamics follows the fixed points determined by the instantaneous fluid-velocity gradients, and our theory for the orientation distribution relates the shape of the distribution to that of the instantaneous fluid-velocity gradients encountered by the settling particle. Our predictions are in excellent agreement with numerical statistical-model simulations, and with simulations using KS turbulence at large Sv and small enough St.

At large Sv the orientation distribution is very narrowly centered around the orientation the settling particle would assume in a quiescent fluid, in the absence of flow. The overdamped theory predicts that the variance of the distribution is proportional to Sv^{-4} for large Sv, and it determines how the prefactor depends on aspect ratio λ of the particle. In the limit $\lambda \to \infty$ the variance was computed in [56].

We demonstrated that the overdamped theory breaks down at finite Stokes numbers, when the settling number exceeds a threshold determined by St. In this regime particle inertia matters. Klett [28] proposed a theory for the orientation variance for nearly spherical particles, taking into account particle inertia in the angular dynamics. His theory assumes that this dynamics is driven by the fluid-velocity gradients experienced by the settling particle, and that these gradients are uncorrelated in time so that diffusion approximations can be applied. Klett's theory predicts that the variance is proportional to Sv^{-2}. In our 2D model simulations we do observe this scaling for very large Sv, so large that the settling time is the smallest time scale of the inertial dynamics. But our results indicate that it is necessary to take into account particle inertia not only in the angular dynamics but also in the centre-of-mass motion to derive a theory from first principles. This gives rise to additional fluctuating terms in the angular equation of motion that are expected to change the orientation variance. More importantly, our simulations also show that particle inertia gives rise to a complex dependence of the orientation variance on particle shape, on the Stokes number, and upon the settling number. When the variance is small, it may be possible to derive a theory for the variance using small-angle approximations. But this remains a question for the future.

Here we applied our theory only to prolate particles. It is of interest to consider oblate particles too, because flat disks and slender rods have qualitatively different shape factors (figure 1). We therefore expect that the effect of particle inertia on the angular dynamics of flat disks can be quite different from that on slender rods.

Also, we considered only the leading order in the inverse settling number, but the overdamped theory allows us to take into account higher-order corrections in this parameter. Such corrections change the relation between the fixed points of the angular dynamics and the fluid-velocity gradients experienced by the particle. This modifies the form of the distribution of n_g, and it may explain the overshooting seen in figure 6(b) at moderate values of Sv, but the details remain to be worked out.

Here we analysed a limit of the problem where the fluid-inertia torque dominates the angular motion. In [5, 6, 47–49], by contrast, this torque was neglected. The question is thus whether one can find regions where inertial torque does not dominate. This is considered in [62]. The simulations described there show that the fluid-inertia torque can be smaller than Jeffery's torque only when Re_λ is small. In a very turbulent flow, when Re_λ is large, the torque induced by fluid inertia is always dominant. More precisely, when the ratio of the correlation length over the Kolmogorov length is large, $\ell/\eta_\mathrm{K} \propto \mathrm{Re}_\lambda^{1/2} \gg 1$, then the only possible orientation bias corresponds to non-spherical particles settling with their broad sides down, the limit considered here.

The experiments measuring the orientations of rods settling in a vortex flow described in [51] are performed in the overdamped limit. In the future we intend to apply the theory outlined in section 4 to spheroids settling in a 2D vortex flow, using the fact that the fixed points of the angular dynamics can be found explicitly as functions of the fluid-velocity gradients in two spatial dimensions. We will analyse the effect of particle shape by considering the angular dynamics of flat disks settling in such flows. Figure 1 indicates that the behaviour could be quite different from that of rods, because the shape factors are so different. This 2D system is well suited to study the effects of finite Stokes numbers in more detail, because the 2D dynamics is much simpler than the three-dimensional turbulent dynamics.

The overdamped theory (equation (38)) assumes that Sv is large, and that St is small enough. Since $\mathrm{Sv} = \mathrm{St}\, g\tau_\mathrm{K}^2/\eta_\mathrm{K} = \mathrm{St}/\mathrm{Fr}$, this requires some discussion. Here $\mathrm{Fr} = \eta_\mathrm{K}/(g\tau_\mathrm{K}^2)$ is the Froude number [60]. We conclude that the Froude number must be small for the overdamped theory to work quantitatively. In turbulence $\mathrm{Fr} \sim \mathscr{E}^{3/4}/(g\nu^{1/4})$ where $\mathscr{E}$ is the dissipation rate per unit mass. Using $\nu \sim 10^{-5}\ \mathrm{m^2\ s^{-1}}$ and $g = 10\ \mathrm{m\ s^{-2}}$ we find that Fr ranges from 0.002 at $\mathscr{E} = 1\ \mathrm{cm^2\ s^{-3}}$ to 0.3 at $\mathscr{E} = 1000\ \mathrm{cm^2\ s^{-3}}$. So we require modest values of the dissipation rate per unit mass, $\mathscr{E}$, for the theory to work quantitatively. This is the limit where gravity dominates over the turbulent fluctuations, the limit we intended to describe.

In the future it is necessary to address possible shortcomings of our model which approximates the inertial contributions to force and torque by those for a homogeneous steady flow. Even in the steady case it remains an open question how to model the torque when Re_p and $\sqrt{\mathrm{Re}_s}$ are of the same order, even if both dimensionless numbers are small. Furthermore, turbulent flow is unsteady. While it is common practice to use steady approximations for the instantaneous force and torque (as we do here) it is not known how to compute contributions to the torque due to unsteadiness for general inhomogeneous flows. We expect that the methods presented in [44] can be generalised to treat at least spatially linear, unsteady flows. Finally, to justify our model for the inertial torque it is necessary that Re_p is small. At the same time we assumed that Sv is large. From the definitions (9) and (15) of these dimensionless numbers we see that $\mathrm{Re}_p = (a/\eta_\mathrm{K})(\mathrm{Sv}/A_\perp)$. To satisfy both requirements we must therefore assume the particles to be much smaller than the Kolmogorov length. Since $\eta_\mathrm{K} \sim (\nu^3/\mathscr{E})^{1/4}$ this condition is more easily met when $\mathscr{E}$ is small. In the slender-body limit, Khayat and Cox [25] obtained an improved approximation for the inertial torque, valid for larger Re_p, which was tested in [51] and was found to agree better with the experiments at larger Re_p. But corresponding corrections for other particle shapes are not yet known.

Acknowledgments

BM and AP thank E Guazzelli for enlightening discussions. KG and BM were supported by the grant *Bottlenecks for particle growth in turbulent aerosols* from the Knut and Alice Wallenberg Foundation, Dnr. KAW 2014.0048, and in part by VR Grant No. 2017-3865. AP and AN acknowledge support from the IDEXLYON project (Contract ANR-16-IDEX-0005) under University of Lyon auspices. Computational resources were provided by C3SE and SNIC, and PSMN.

References

[1] Pruppacher H R and Klett J D 1997 *Microphysics of Clouds and Precipitation* 2nd edn (Dordrecht: Kluwer) p 954
[2] Evans K F, Walter S J, Hemusfield A J and Deeter M N 1998 Modelling of submillimeter passive remote sensing of cirrus clouds *J. Appl. Meteorol.* **37** 183
[3] Noel V and Chepfer H 2010 A global view of horizontally oriented crystals in ice clouds from Cloud-Aerosols Lidar and Infrared Pathfinder satellite observation (CALIPSO) *J. Geophys. Res.* **115** D00H23
[4] Okamoto H, Sato K and Hagihara Y 2010 Global analysis of ice microphysics from CloudSat and CALIPSO: incorporation of specular reflection in lidar signals *J. Geophys. Res.* **115** D22209
[5] Siewert C, Kunnen R P J and Schrőder W 2014 Collision rates of small ellipsoids settling in turbulence *J. Fluid Mech.* **758** 686–701
[6] Jucha J, Naso A, Lévêque E and Pumir A 2018 Settling and collision between small ice crystals in turbulent flows *Phys. Rev. Fluids* **3** 014604
[7] Kiørboe T 2001 Formation and fate of marine snow: small-scale processes with large-scale implications *Sci. Mar.* **65** 57–71
[8] Ruiz J, Macías D and Peters F 2004 Turbulence increases the average settling velocity of phytoplankton cells *PNAS* **101** 17720–4
[9] Cencini M, Boffetta G, De Lillo F, Stocker R, Barry M, Durham W M and Climent E 2013 Turbulence drives microscale patches of motile phytoplankton *Nat. Commun.* **4** 2148
[10] Gustavsson K, Berglund F, Jonsson P R and Mehlig B 2016 Preferential sampling and small-scale clustering of gyrotactic microswimmers in turbulence *Phys. Rev. Lett.* **116** 108104
[11] Marchioli C, Fantoni M and Soldati A 2010 Orientation, distribution, and deposition of elongated, inertial fibers in turbulent channel flow *Phys. Fluids* **22** 033301
[12] Maxey M R and Corrsin S 1986 Gravitational settling of aerosol particles in randomly oriented cellular flow fields *J. Atmos. Sci.* **43** 1112–34
[13] Maxey M R 1987 The gravitational settling of aerosol particles in homogeneous turbulence and random flow fields *J. Fluid Mech.* **174** 441–65
[14] Wang L and Maxey M R 1993 Settling velocity and concentration distribution of heavy particles in homogeneous isotropic turbulence *J. Fluid Mech.* **256** 27–68
[15] Good G H, Ireland P J, Bewley G P, Bodenschatz E, Collins L R and Warhaft Z 2014 Settling regimes of inertial particles in isotropic turbulence *J. Fluid Mech.* **759** R3
[16] Petersen A J, Baker L and Coletti F 2019 Experimental study of inertial particles clustering and settling in homogeneous turbulence *J. Fluid Mech.* **864** 925–70
[17] Ardekani M N, Costa P, Breugem W P and Brandt L 2016 Numerical study of the sedimentation of spheroidal particles *Int. J. Multiph. Flow* **87** 16–34
[18] Fornari F, Zade S, Brandt L and Picano F 2019 Settling of finite-size particles in turbulence at different volume fractions *Acta Mech.* **230** 413
[19] Gustavsson K, Vajedi S and Mehlig B 2014 Clustering of particles falling in a turbulent flow *Phys. Rev. Lett.* **112** 214501
[20] Bec J, Homann H and Ray S S 2014 Gravity-driven enhancement of heavy particle clustering in turbulent flow *Phys. Rev. Lett.* **112** 184501
[21] Ireland P J, Bragg A D and Collins L R 2016 The effect of Reynolds number on inertial particle dynamics in isotropic turbulence: II. Simulations with gravitational effects *J. Fluid Mech.* **796** 659–711
[22] Mathai V, Calzavarini E, Brons J, Sun C and Lohse D 2016 Microbubbles and microparticles are not faithful tracers of turbulent acceleration *Phys. Rev. Lett.* **117** 024501
[23] Parishani H, Ayala O, Rosa B, Wang L-P and Grabowski W W 2015 Effects of gravity on the acceleration and pair statistics of inertial particles in homogeneous isotropic turbulence *Phys. Fluids* **27** 033304
[24] Cox R G 1965 The steady motion of a particle of arbitrary shape at small Reynolds numbers *J. Fluid Mech.* **23** 625–43

[25] Khayat R E and Cox R G 1989 Inertia effects on the motion of long slender bodies *J. Fluid Mech.* **209** 435–62
[26] Dabade V, Marath N K and Subramanian G 2015 Effects of inertia and viscoelasticity on sedimenting anisotropic particles *J. Fluid Mech.* **778** 133–88
[27] Candelier F and Mehlig B 2016 Settling of an asymmetric dumbbell in a quiescent fluid *J. Fluid Mech.* **802** 174–85
[28] Klett J D 1995 Orientation model for particles in turbulence *J. Atmos. Sci.* **52** 2276–85
[29] Jeffery G B 1922 The motion of ellipsoidal particles immersed in a viscous fluid *Proc. R. Soc.* A **102** 161
[30] Pumir A and Wilkinson M 2011 Orientation statistics of small particles in turbulence *New J. Phys.* **13** 093030
[31] Parsa S, Calzavarini E, Toschi F and Voth G A 2012 Rotation rate of rods in turbulent fluid flow *Phys. Rev. Lett.* **109** 134501
[32] Chevillard L and Meneveau C 2013 Orientation dynamics of small, triaxial-ellipsoidal particles in isotropic turbulence *J. Fluid Mech.* **737** 571
[33] Gustavsson K, Einarsson J and Mehlig B 2014 Tumbling of small axisymmetric particles in random and turbulent flows *Phys. Rev. Lett.* **112** 014501
[34] Byron M, Einarsson J, Gustavsson K, Voth G A, Mehlig B and Variano E 2015 Shape-dependence of particle rotation in isotropic turbulence *Phys. Fluids* **27** 035101
[35] Zhao L, Challabotla N R, Andersson H I and Variano E A 2015 Rotation of nonspherical particles in turbulent channel flow *Phys. Rev. Lett.* **115** 244501
[36] Voth G 2015 Disks aligned in a turbulent channel *J. Fluid Mech.* **772** 1
[37] Voth G and Soldati A 2017 Anisotropic particles in turbulence *Annu. Rev. Fluid Mech.* **49** 249–76
[38] Fries J, Einarsson J and Mehlig B 2017 Angular dynamics of small crystals in viscous flow *Phys. Fluids* **2** 014302
[39] Einarsson J, Angilella J R and Mehlig B 2014 Orientational dynamics of weakly inertial axisymmetric particles in steady viscous flows *Physica* D **278-279** 79–85
[40] Saffman P G 1956 On the motion of small spheroidal particles in a viscous liquid *J. Fluid Mech.* **1** 540–53
[41] Subramanian G and Koch D L 2005 Inertial effects on fibre motion in simple shear flow *J. Fluid Mech.* **535** 383–414
[42] Einarsson J, Candelier F, Lundell F, Angilella J R and Mehlig B 2015 Rotation of a spheroid in a simple shear at small Reynolds number *Phys. Fluids* **27** 063301
[43] Rosén J, Einarsson T, Nordmark A, Aidun C K, Lundell F and Mehlig B 2015 Numerical analysis of the angular motion of a neutrally buoyant spheroid in shear flow at small Reynolds numbers *Phys. Rev.* E **92** 063022
[44] Candelier F, Mehlig B and Magnaudet J 2019 Time-dependent lift and drag on a rigid body in a viscous steady linear flow *J. Fluid Mech.* **864** 554–95
[45] Saffman P G 1965 The lift on a small sphere in a slow shear flow *J. Fluid Mech.* **22** 385
[46] Saffman P G 1968 Corrigendum to: the lift on a small sphere in a slow shear flow *J. Fluid Mech.* **31** 624
[47] Siewert C, Kunnen R P J, Meinke M and Schröder W 2014 Orientation statistics and settling velocity of ellipsoids in decaying turbulence *Atmos. Res.* **142** 45–56
[48] Gustavsson K, Jucha J, Naso A, Lévêque E, Pumir A and Mehlig B 2017 Statistical model for the orientation of nonspherical particles settling in turbulence *Phys. Rev. Lett.* **119** 254501
[49] Naso A, Jucha J, Lévêque E and Pumir A 2018 Collision rate of ice crystals with water droplets in turbulent flows *J. Fluid Mech.* **845** 615
[50] Candelier F, Einarsson J and Mehlig B 2016 Rotation of a small particle in turbulence *Phys. Rev. Lett.* **117** 204501
[51] Lopez D and Guazzelli E 2017 Inertial effects on fibers settling in a vortical flow *Phys. Rev. Fluids* **2** 024306
[52] Kramel S, Tierney L, Rees W, Voth G A, Menon U, Roy A and Koch D L 2016 Orientation statistics of nonspherical particles sedimenting in turbulence *Abstract E28.00002, 69th Annual Meeting of the APS Division of Fluid Dynamics (Portland, Oregon)*
[53] Gustavsson K and Mehlig B 2016 Statistical models for spatial patterns of heavy particles in turbulence *Adv. Phys.* **65** 1
[54] Fung J C H, Hunt J C R, Malik N A and Perkins R J 1992 Kinematic simulation of homogeneous turbulence by unsteady random fourier modes *J. Fluid Mech.* **236** 281–318
[55] Vosskuhle M, Pumir A, Lévêque E and Wilkinson M 2015 Collision rate for suspensions at large Stokes numbers—comparing Navier–Stokes and synthetic turbulence *J. Turbul.* **16** 15–25
[56] Kramel S 2017 Non-spherical particle dynamics in turbulence *PhD Thesis* Wesleyan University
[57] Kim S and Karrila S J 1991 *Microhydrodynamics: Principles and Selected Applications* (Oxford: Butterworth-Heinemann)
[58] Frisch U 1997 *Turbulence* (Cambridge: Cambridge University Press)
[59] Brenner H 1961 The Oseen resistance of a particle of arbitrary shape *J. Fluid Mech.* **11** 604–10
[60] Devenish B J *et al* 2012 Droplet growth in warm turbulent clouds *Q. J. R. Meteorol. Soc.* **138** 1401–29
[61] Lovalenti P M and Brady J F 1993 The force on a bubble, drop or particle in arbitrary time-dependent motion at small Reynolds number *Phys. Fluids* **5** 2104–16
[62] Sheikh M Z, Gustavsson K, Lopez D, Mehlig B, Pumir A and Naso A 2019 Importance of fluid inertia for the orientation of spheroids settling in a turbulent flow arXiv:1904.07575
[63] Schumacher J, Scheel J D, Krasnov D, Donzis D A, Yakhot V and Sreenivasan K R 2014 Small-scale universality in fluid turbulence *Proc. Natl Acad. Sci.* **111** 10961
[64] Buaria D, Pumir A, Bodenschatz E and Yeung P K 2019 Extreme velocity gradients in turbulent flows *New J. Phys.* **21** 043004
[65] Vajedi S, Gustavsson K, Mehlig B and Biferale L 2016 Inertial-particle accelerations in turbulence: a Lagrangian closure *J. Fluid Mech.* **798** 187
[66] Cencini M, Boffetta G, Borgigno M and De Lillo F 2019 Gyrotactic phytoplankton in laminar and turbulent flows: a dynamical systems approach *Eur. Phys. J.* E **42** 31
[67] Biferale L, Gustavsson K and Scatamacchia R 2019 Helicoidal particles in turbulent flows with multi-scale helical injection *J. Fluid Mech.* **869** 646
[68] Calzavarini E, Volk R, Bourgoin M, Lévêque E, Pinton J F and Toschi F 2009 Acceleration statistics of finite-sized particles in turbulent flow: the role of Faxén forces *J. Fluid Mech.* **630** 179
[69] Menon U, Roy A, Kramel S, Voth G and Koch D 2017 Theoretical predictions of the orientation distribution of high-aspect-ratio, inertial particles settling in isotropic turbulence *Abstract Q36.00011, 70th Annual Meeting of the APS Division of Fluid Dynamics (Denver, Colorado)*
[70] Meibohm J and Mehlig B 2019 Heavy particles in a persistent random flow with traps arXiv:1902.04354
[71] Xu H, Pumir A and Bodenschatz E 2011 The pirouette effect in turbulent flows *Nat. Phys.* **7** 709